# Cathodoluminescence studies of chevron features in semi-polar $(11\bar{2}2)$ InGaN/GaN multiple quantum well structures

C. Brasser,[1,a)] J. Bruckbauer,[1] Y. Gong,[2] L. Jiu,[2] J. Bai,[2] M. Warzecha,[3] P. R. Edwards,[1] T. Wang,[2] and R. W. Martin[1]
[1]*Department of Physics, SUPA, University of Strathclyde, Glasgow G4 0NG, United Kingdom*
[2]*Department of Electronic and Electrical Engineering, University of Sheffield, Sheffield S1 3JD, United Kingdom*
[3]*Strathclyde Institute of Pharmacy and Biomedical Sciences, University of Strathclyde, Glasgow G4 0RE, United Kingdom*

(Received 9 January 2018; accepted 5 April 2018; published online 1 May 2018)

Epitaxial overgrowth of semi-polar III-nitride layers and devices often leads to arrowhead-shaped surface features, referred to as chevrons. We report on a study into the optical, structural, and electrical properties of these features occurring in two very different semi-polar structures, a blue-emitting multiple quantum well structure, and an amber-emitting light-emitting diode. Cathodoluminescence (CL) hyperspectral imaging has highlighted shifts in their emission energy, occurring in the region of the chevron. These variations are due to different semi-polar planes introduced in the chevron arms resulting in a lack of uniformity in the InN incorporation across samples, and the disruption of the structure which could cause a narrowing of the quantum wells (QWs) in this region. Atomic force microscopy has revealed that chevrons can penetrate over 150 nm into the sample and quench light emission from the active layers. The dominance of non-radiative recombination in the chevron region was exposed by simultaneous measurement of CL and the electron beam-induced current. Overall, these results provide an overview of the nature and impact of chevrons on the luminescence of semi-polar devices. © *2018 Author(s). All article content, except where otherwise noted, is licensed under a Creative Commons Attribution (CC BY) license (http://creativecommons.org/licenses/by/4.0/).* https://doi.org/10.1063/1.5021883

## I. INTRODUCTION

The semi-polar growth of III-nitrides provides a route to increase device efficiency by reducing the built-in electric fields present along polar growth directions.[1] These orientations may also provide a way to bridge the "green gap," a well-known limitation of the III-nitrides.[2] Furthermore, some semi-polar planes, such as $(11\bar{2}2)$, have binding sites that may accommodate indium atoms more easily[3] than others, allowing higher crystal quality for the same emission wavelength.[4] Consequently, III-nitride devices with long wavelength emission can be achieved using semi-polar growth.[5,6] However, semi-polar growth introduces a new range of growth imperfections, including arrow-head features often referred to as "chevrons."[7–9] Both planar and patterned substrates have been used to achieve semi-polar growth, and these different growth techniques have an impact on the chevron formation.[10,11] For growth on planar substrates, the formation of chevrons has been attributed to interference between undulations along the $[11\bar{2}\bar{3}]$ and $[1\bar{1}00]$ directions, which in turn occur due to anisotropic surface diffusion.[12] For samples grown using epitaxial lateral overgrowth (ELOG) methods, where a patterned substrate or template is used, there is an additional effect causing the chevrons to appear more pronounced.[13] This arises from the differing growth rates along the *c*- and *a*-growth directions, which results in irregularities during their coalescence.[8] The chevrons are undesirable, due to disruption of the crystal structure, and methods have been investigated to reduce their formation. Some have varied the growth conditions, such as temperature and pressure, on which the adatom surface diffusion depends, to minimise their formation.[12] Another technique is to use chemical mechanical polishing to reduce the surface roughness, before growing additional layers. This was seen to nearly eliminate chevrons from the following layers when grown in nitrogen-ambient growth conditions.[14] The optical properties of the chevrons have been explored using photoluminescence (PL),[15] but additional information is offered by cathodoluminescence (CL) hyperspectral imaging,[16,17] with its higher spatial resolution. This paper exploits this technique to explore the effect of chevrons on the light emission using two very different structures, namely, a blue-emitting multiple quantum well (MQW) structure and an as-grown and fully processed amber light-emitting diode (LED). Atomic force microscopy (AFM) has been used to investigate the chevron morphology, and simultaneous measurements of CL and electron beam-induced current (EBIC) have provided information on the activity of the charge carriers around the active region of the fully processed LED.

## II. METHODOLOGY

The semi-polar samples were produced using different approaches to overgrowth involving random or ordered masks. All samples studied in this paper were grown by metal organic chemical vapour deposition (MOCVD) on an

a)Electronic mail: catherine.brasser@strath.ac.uk

 © Author(s) 2018.

*m*-plane $(10\bar{1}0)$ sapphire substrate. The blue MQW sample began with a high temperature (HT) 200 nm AlN buffer layer,[18] followed by a 1.3 $\mu$m GaN layer. Next a $SiO_2$ layer is deposited on the GaN layer, followed by a Ni layer. A thermal annealing step then produced Ni nano-islands to form a self-organised Ni mask. Etching was used to form $SiO_2$ nanorods, which were used as a second mask to etch GaN nanorods with a diameter of around 300 nm. The nanorods served as a template for overgrowth of semi-polar GaN which began from the sidewalls of the nanorods, coalesced and continued until a 4 $\mu$m layer thickness was reached. Subsequently five periods of InGaN/GaN quantum wells (QWs) were grown with 10 nm thick GaN barriers and 2.2 nm thick InGaN wells with an 18% InN content.[19,20] The amber-emitting LEDs started with a 1.3 $\mu$m layer of GaN grown on top of a HT AlN buffer layer. Deposition of a layer of $SiO_2$ followed, which was patterned into a regular array of disks using standard lithography. Dry etching was used to produce $SiO_2$ microrods, which act as a second mask for the etching of GaN microrods in a regular array. GaN overgrowth begins from the sidewalls of the microrods, along the [0001] direction and the $[11\bar{2}0]$ direction. Growth continues in these directions until they coalesce, and then continued to a thickness of 5 $\mu$m. After that the LED structure was grown, which includes a 1 $\mu$m *n*-GaN layer, three periods of InGaN/GaN QWs, and was finished with a 150 nm layer of *p*-GaN. The InN content of the InGaN QWs is 40% to achieve light emission in the amber spectral region and the well and barrier widths are 3.8 nm and 7.8 nm (nominal values), respectively. LEDs were fabricated by etching down to the *n*-GaN to apply a Ti/Au *n*-contact, and applying a Ti/Au *p*-contact above a layer of indium tin oxide (ITO), used to assist current spreading.[21] The samples were analysed using a variable pressure scanning electron microscope (SEM) to which a custom-built CL system has been added.[22,23] The axis of the light collection optics is situated at 90° with respect to the electron beam, and the sample is tilted by 45°. The light emitted at room temperature is collected by a reflecting objective and focussed on to the entrance slit of a spectrograph, and the light is detected using an electron multiplying charged coupled device. The beam scans across the sample surface, and a 1600 pixel emission spectrum from 300 to 800 nm is recorded for every pixel with a spatial resolution approaching 10 nm.[24] Electron beam energies of up to 10 kV have been used to probe light emission from up to 300 nm below the sample surface. This depth was calculated by Monte Carlo simulations using the CASINO[25] software to estimate the beam voltages required to excite the active regions of the samples. For contacted LEDs, it is possible to simultaneously probe the light emission and the EBIC in a sample. When the carriers generated by the electron beam reach the active region, one of three processes can occur: radiative recombination (CL), non-radiative recombination, or a flow of current. Therefore, the EBIC signal, measured via an external circuit, provides a pathway to investigate the non-radiative recombination occurring in a sample when correlated with the CL.[26,27] AFM was carried out, in PeakForce tapping mode, on the samples to provide additional information about their surface morphology.

## III. RESULTS AND DISCUSSION

Chevrons are widespread but their size and shape depend on the growth conditions, and therefore vary between samples. The secondary electron (SE) images in Fig. 1 show an example of a chevron from both the blue-emitting MQW sample (*a*) and the amber-emitting as grown LED (*c*).

While both chevrons have a length in the region of 20 $\mu$m, they have very different shapes. It is evident that in the MQW sample the chevron is short and wide, with an opening angle of around 15°, whereas the chevron on the surface of the LED has an opening angle of 10°, appearing longer and narrower. The sizes vary throughout each sample, but the shapes of the chevrons are similar within each sample. Ploch *et al*. have shown a correlation between the opening angles of the chevrons with the growth temperature, namely, wider angles with higher temperatures.[12] Figure 1(b) shows a schematic of a chevron, following the rounded structure of those appearing in the MQW sample. The sides of the structure have been labelled as the "arms," the point of the chevron as the "tip," and the area protruding from the tip as the "tail." The facets along the chevron arms are also quite different: Fig. 1(a) shows smooth facets meeting at a rounded tip, whereas the chevron arms of the LED are rough and meet at a sharp point. The orientation of these facets has been reported as $\{10\bar{1}1\}$.[28] The structure of the tail is also variable and in some chevrons no tail is evident.

The CL imaging results, measured at 5 kV, of a chevron and its surrounding region in the blue-emitting MQW sample are shown in Fig. 2. The sample exhibited a complex luminescence behaviour with three separate peaks occurring within the sample. These peaks are identified and their corresponding positions are shown on the SE image in Fig. 2(a),

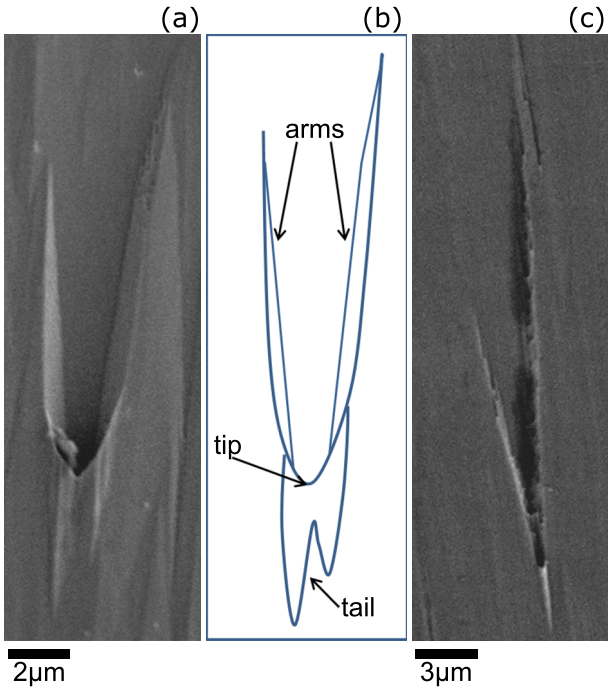


FIG. 1. Chevron structures: SE image of a typical chevron from the blue-emitting MQW sample (a) and from the amber-emitting LED (c). A schematic of a chevron is shown in (b).

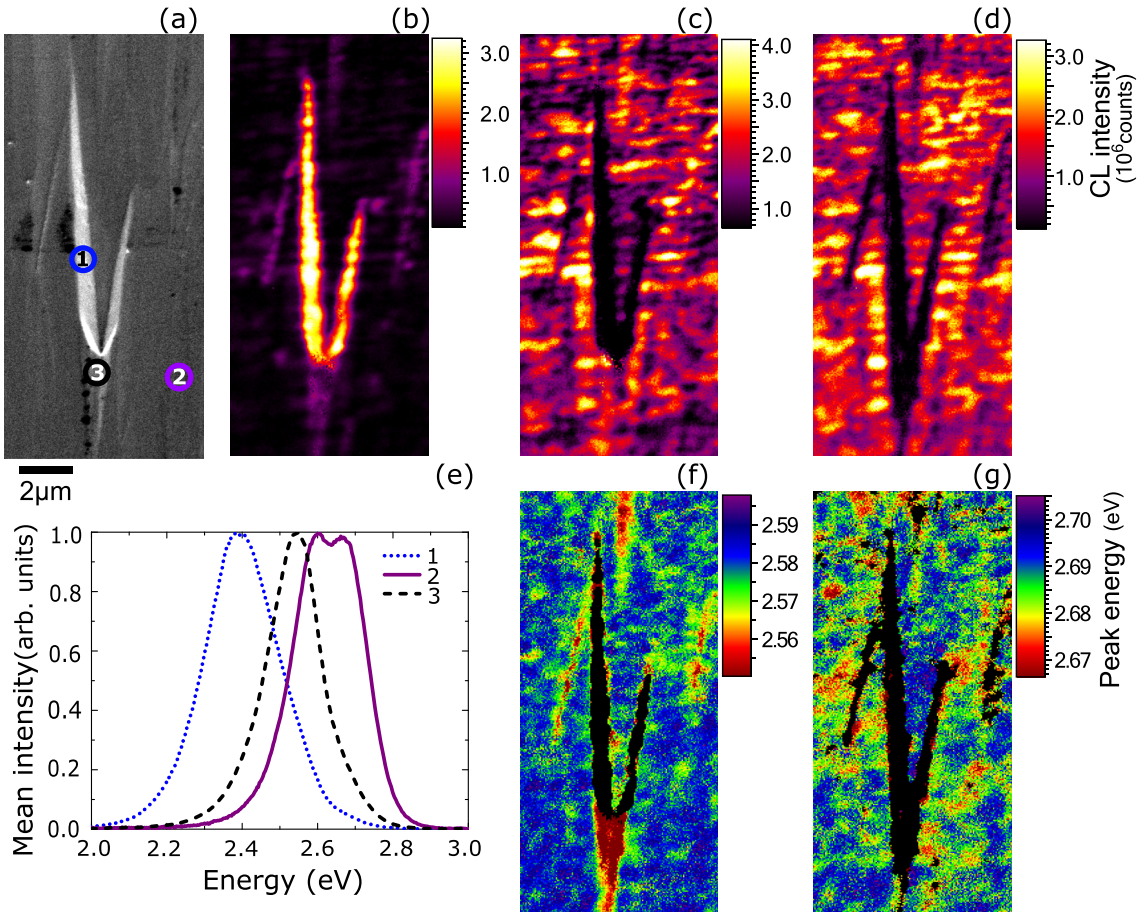


FIG. 2. SE image (a), and CL intensity images of the fitted peaks near 2.4 eV (b), 2.6 eV (c) and 2.7 eV (d) of a chevron occurring in the blue MQW sample. Normalised CL spectra from the arms (1), tail (3), and the area surrounding (2) the chevron are shown in (d). CL peak energy images of the lower and higher energy end of the double peak are shown in (f) and (g), respectively.

which relate to the spectra shown in Fig. 2(e). Point 1 is located on the arm of the chevron and the emission is considerably broader and redshifted by 200 meV when compared to the emission in the area surrounding the chevron, marked by point 2. The typical luminescence of the surrounding area has two peaks near 2.6 eV and 2.7 eV. The intensities of these two peaks varied across the sample, and the higher energy peak disappeared when the surface of the sample was in any way disturbed. An example of the disrupted structure is marked by point 3, on the tail of the chevron. Here, the lower energy peak alone remains and is redshifted by around 50 meV with respect to the emission from the undisturbed surface. These peaks were fitted using three Gaussian functions, and the corresponding CL intensity images are shown in Figs. 2(b)–2(d) in order of increasing energy. Viewing these along with the SE image, the lower energy peak appears exclusively along the arms of the chevron [Fig. 2(b)], and the highest energy peak [Fig. 2(d)] disappears where the surface is disturbed. The arms of the chevron appear to have a different semi-polar orientation, and therefore are expected to have a different rate of InN incorporation,[29–31] than the majority of the sample, which could account for this considerable redshift. A similar shift has been seen in chevrons for samples with comparable emission energy in Ref. 32. The arm emission is in a different spectral region, which makes this sample undesirable for many LED applications which require monochromatic light. The area surrounding the chevron exhibits a lack of uniformity, with a random distribution of brighter and darker areas. This can be explained by the nature of the sample template, namely, a randomly distributed array of nanorods. The two components of the double peak show shifts as seen in the CL peak energy images of these peaks, Figs. 2(f) and 2(g). The black areas in these images are masked data as these sections do not exhibit these peaks. The highest energy peak [Fig. 2(f)] emission is blueshifted within the chevron compared to the surrounding areas. This could be due to a narrowing of the QWs caused by the disruption of the sample surface by the chevron. Southern-Holland *et al.*[15] have investigated similar chevrons using photoluminescence. They identify a redshift at what they refer to as the "join" of the chevron. The high spatial resolution of the CL technique has identified this redshift occurring at the tail rather than the tip of the chevron. The tail of the chevron may have a different semi-polar orientation than the rest of the structure, including the arms, which would result in a different incorporation of InN, and hence change the emission wavelength.

Figure 3(a) shows an SE image of a chevron occurring in the amber LED sample. CL hyperspectral imaging was carried out on this area and Figs. 3(b)–3(e) display the results. The electron beam, operating at 10 kV, travelled through the QWs and penetrated slightly into the *n*-GaN

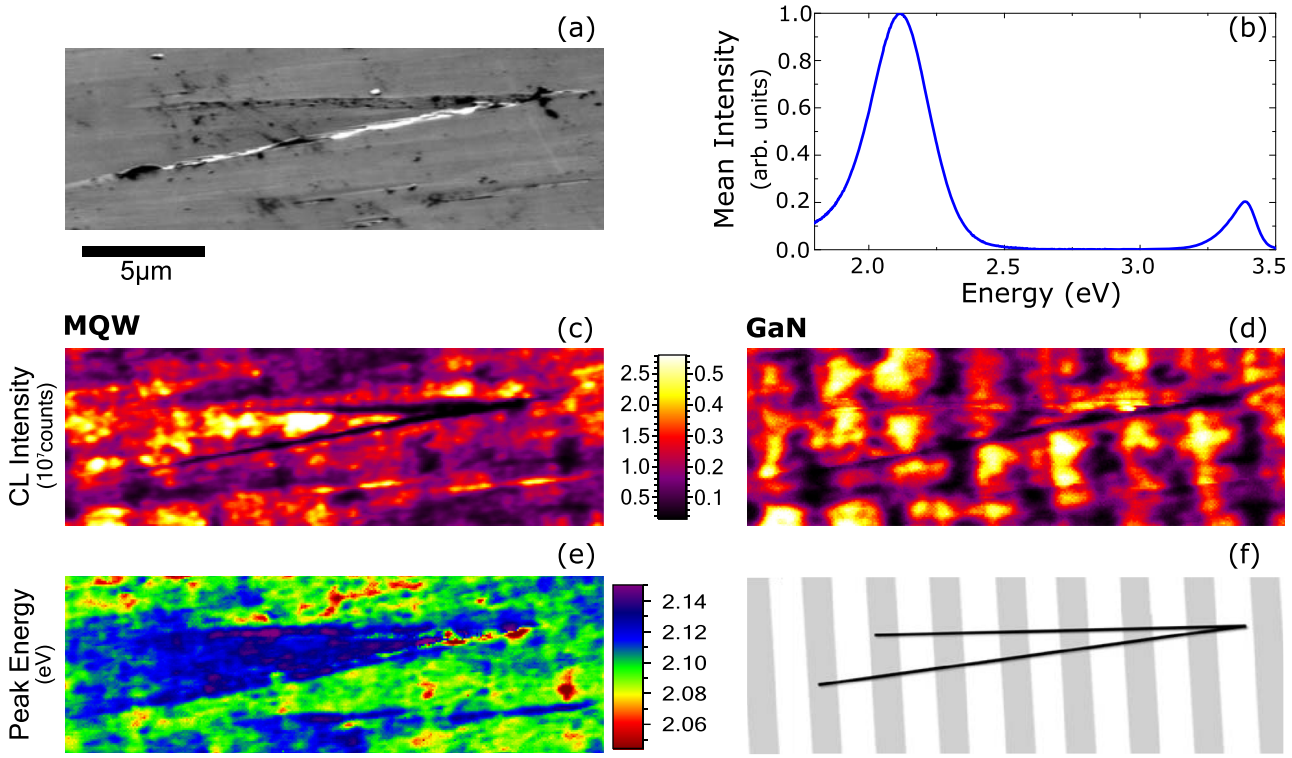


FIG. 3. A chevron from the amber LED as seen in the SE image (a), with the mean CL spectrum from the area in (b). Maps of the CL QW emission intensity (c) and GaN emission intensity (d) and the QW peak energy (e) are subsequently shown. A schematic of the chevron, including the stripes of low and high BSF regions, is shown in (f).

layer beneath, exciting light emission from both the active region and the GaN below. This is demonstrated in the mean spectrum from this map in Fig. 3(b), showing an intense MQW peak centred at 2.11 eV in the amber spectral region, and a smaller peak corresponding to near band edge (NBE) emission of GaN near 3.4 eV. By fitting these peaks to Gaussian and Voigt functions, respectively, it was possible to plot separate CL images of their behaviour. The QW and GaN emission intensity maps are shown in Figs. 3(c) and 3(d), respectively. The QW emission shows a drop in intensity on both arms and at the tip of the chevron, increasing towards the tip. This drop in intensity is only seen along the lower arm in the GaN emission. The GaN has pronounced stripes of high and low intensity perpendicular to the chevron, which are not so prominent, though visible, in the QW emission. Figure 3(f) is a schematic of the chevron with these stripes. The QW energy map is displayed in Fig. 3(e) which again shows a blueshift within the chevron, but also reveals a blueshift along the arms. Comparing the QW and GaN emission, it is clear that the chevron has a much larger impact on the MQW intensity, evidenced by a considerable drop in intensity along the arms which is not as evident in the GaN. This drop could be due to a lower crystal quality in this region, or that the quantum-confined Stark effect (QCSE) plays a larger part in these planes, reducing the electron and hole wave-function overlap and hence the overall radiative recombination; however, it could also be due to an increase in InN content not present in the GaN. The light is collected in the direction looking from the top of the image, so the alignment of the optics to the surface disruption should also be considered as a factor for the reduction in intensity. However, if this was the sole reason, there would not be the discrepancy between the QW and the GaN emission. The stripes of low and high intensity perpendicular to the chevron have a periodicity relating to the microrod template, but this has been more fully explored elsewhere.[21] They indicate areas of material with a high number of basal plane stacking faults (BSFs) and those with much fewer. The overgrowth from the patterned template begins from the sides of the microrods, in both the polar *c*-direction and non-polar *a*-directions. The growth along the polar direction is virtually free of dislocations, whereas the non-polar *a*-direction has many extended defects. As the polar growth rate is larger than the one in *a*-direction, the BSFs from the non-polar *a*-direction are blocked by the polar growth, resulting in stripes of BSF dense and sparse regions. These stripes are visible in the QW intensity image, but less pronounced. This could be due to some factor limiting propagation of the BSFs into the QW region at the *n*-GaN/QW barrier growth boundary, or the InGaN/GaN boundaries in the QW region. The map of peak energy of the QW emission also reveals changes in the chevron area. A blueshift in the energy of around 30 meV is apparent within the chevron and a further 10 meV shift occurs along its arms. There are a number of reasons for these increases in emission energy. The disruption of the crystal structure in the chevron region could result in a change in the overall strain in the material, and/or could cause a narrowing of the QWs, leading to a blueshift. The different planes introduced along the chevron arms could also be less accommodating to the larger In atoms, reducing the overall InN content and shortening the wavelength.

To further investigate the morphology of chevrons, AFM was performed on the as-grown LED, and the results

are shown in Fig. 4. This displays an undulating surface with alternating striations parallel to the chevron with a height difference of approximately 90 nm. These striations are not to be confused with the stripes in Fig. 3, which are perpendicularly oriented. The red and blue lines parallel and perpendicular to the chevron represent linescans corresponding to the lines on the graph in Fig. 4(b). This graph identifies that the chevron slopes down towards the tip, to a depth of at least 170 nm below the surface. This clarifies the results from Fig. 3, namely, the reduction in QW emission intensity towards the tip of the chevron. The active region of the LED is compromised by the chevron disturbing its structure, so the light-emitting area of the device is disrupted. Although the chevrons are formed during the overgrowth and propagate throughout the device, they have the most impact at the surface, quenching the QW luminescence more than that from the *n*-GaN below.

It is important to note that in different semi-polar structures, chevrons take varied forms and hence have a different impact on the luminescence of devices. For this reason, two very different structures were chosen for investigation. One sample has the full LED structure, whereas the other has no p–n junction surrounding its MQWs. The two samples have very different emission wavelengths, and one is grown on a regular array of microrods whereas the other has a random nanorod template. Exploiting these differences gives a broader overview of the chevrons impact on luminescence. For example, the blue-emitting MQW sample from Fig. 2 does not exhibit the same drop in intensity along the arms of the chevron as the amber LED. This is likely a result of the close-packed template limiting the penetration of the chevrons into the structure. There appears to be an important changeover in the effects driving the wavelength shift (either change in relative InN incorporation or well width). For a higher average InN content, as in the amber LED sample, it is postulated that the chevron arms incorporate relatively less InN, or have decreased QW thickness, compared with the $(11\bar{2}2)$ plane whilst the opposite is true in the blue MQW sample with lower average InN content. It has been reported that InN incorporation rates are different for different semi-polar facets.[29,33] However the energy shift within each chevron is in the same direction, that is, towards a higher energy, which could be due to structural changes, such as a narrowing of the QWs.

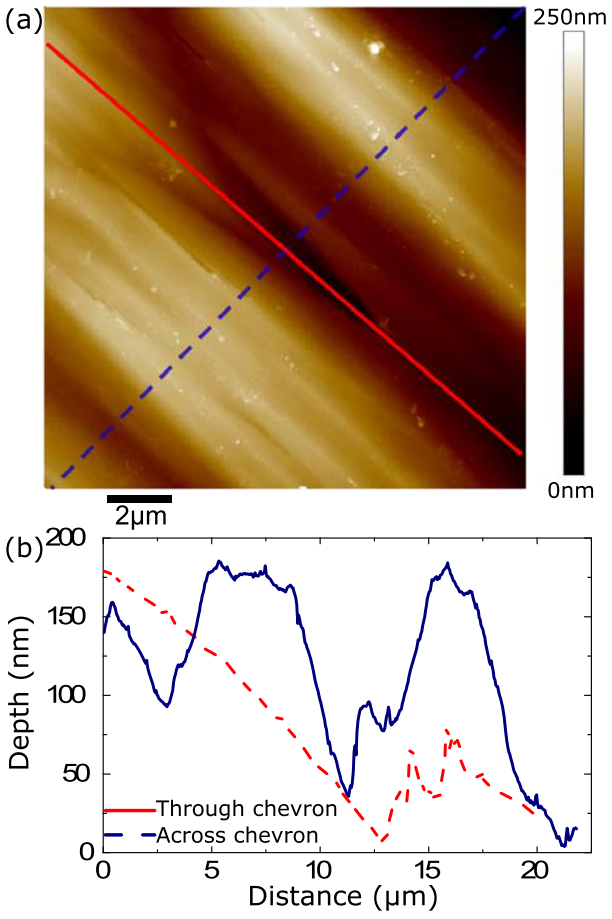


FIG. 4. AFM image of a chevron in the unprocessed LED (a) and a graph showing a depth measurement across and through the chevron (b).

To explore the effect of chevrons on a working device, simultaneous CL and EBIC maps were taken of a processed amber LED with the same sample structure as in Fig. 3. The SE image, QW energy, EBIC signal, and QW emission intensity, taken using a ∼2nA electron beam, are shown in Figs. 5(a)–5(d), respectively. The chevrons in this sample are often less defined as the ITO current spreading layer is applied when processing the as-grown LED into a working device. However, it is evident that although the chevrons may be somewhat buried and appear less pronounced, they still impact the luminescence of device in the same way. For example, the blueshifts in the chevron region shown in Fig. 5(b) are similar to those in Fig. 3(e) although the disparity between the blueshifts along the arms and within the chevron is clearer here. Figure 5(d) also shows a definite drop in QW emission intensity along the chevron arms. There is also a drop in the EBIC measured along the arms of the chevron as seen in Fig. 5(c). The EBIC signal is reduced by both radiative and non-radiative recombination. This demonstrates that the reduction in intensity of the CL in this region was not primarily due to the leakage of carriers, but rather due to non-radiative recombination dominating in this region.[26,27] Similarly, there is a correlation between the EBIC and CL intensity in the stripes with high BSF density, namely, small current and low intensity, leading to the conclusion that the BSFs do not provide a current path, but rather act as non-radiative recombination centres. There is also a 30 meV difference in peak energy of the QW emission between the unprocessed sample in Fig. 3 and the contacted sample shown above. When the device is in open circuit condition, or similarly when an LED is unprocessed, the charge which drifts out of the depletion region has no path by which to escape, and therefore accumulates at either end of the depletion region. This buildup of charge produces an electric field across the QWs, and consequently changes their emission energy.[26,27]

## IV. CONCLUSIONS

In conclusion, the structural and luminescent properties of chevrons occurring in two semi-polar structures for light emission have been investigated, and the results highlight a

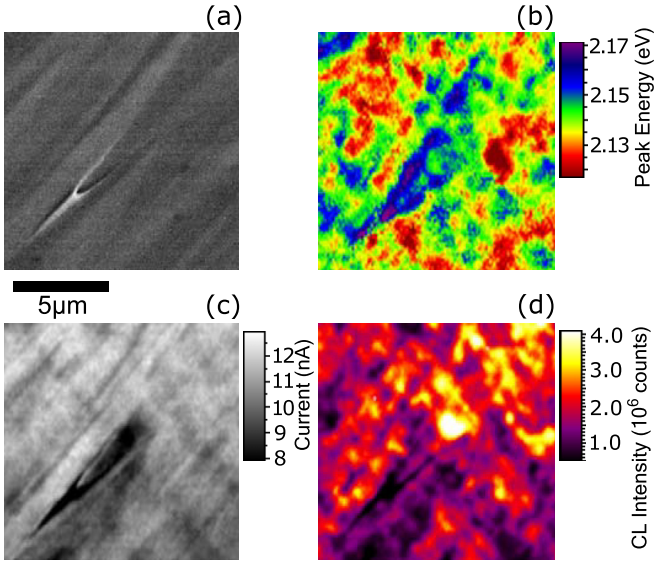


FIG. 5. SE (a), CL peak energy (b), electron beam-induced current (c), and CL intensity (d) images of a chevron in the fully processed amber LED.

range of ways chevrons can impact device performance. The new planes introduced by the chevron into the structure result in a lack of uniformity in the InN incorporation in their region. In the blue MQW sample, this spread resulted in a large redshift in the emission along the arms of the chevron, but in the amber LED, which had a much higher overall concentration of InN in the QW, the emission along the chevron arms was blueshifted. In both samples, the region of the chevron between the arms exhibited a slight blueshift in the light emission; it has been suggested that this is caused by a narrowing of the QWs as a result of the crystal structure being disrupted. AFM mapping showed the extent by which the chevrons can impact the structure, penetrating over 150 nm into the sample, and quenching light emission from the LED. Simultaneous CL-EBIC studies of the amber LED highlighted that the chevron features included many non-radiative recombination centres along the arms. Overall, these results give a broad overview of the nature and impact of chevrons, by investigating two very different semi-polar samples using complementary microscopy techniques.

## ACKNOWLEDGMENTS

The authors would like to thank UK EPSRC (Grant Nos. EP/L016982/1, EP/M003132/1 and EP/M015181/1) for financial support. AFM measurements were carried out in the CMAC National Facility, housed within the University of Strathclyde's Technology and Innovation Centre, and funded with a UKRPIF (UK Research Partnership Institute Fund) capital award (SFC ref. H13054) from the Higher Education Funding Council for England (HEFCE). Data associated with this research are available at http://dx.doi.org/10.15129/f5c701c4-ca09-495b-be4a-faf44710629f.

[1]H. A. T. Takeuchi and I. Akasaki, Jpn. J. Appl. Phys., Part 1 **39**, 413 (2000).
[2]Y. Zhao, S. H. Oh, F. Wu, Y. Kawaguchi, S. Tanaka, K. Fujito, J. S. Speck, S. P. DenBaars, and S. Nakamura, Appl. Phys. Express **6**, 062102 (2013).
[3]R. M. Farrell, E. C. Young, F. Wu, S. P. DenBaars, and J. S. Speck, Semicond. Sci. Technol. **27**, 024001 (2012).
[4]Y. Zhao, Q. Yan, C.-Y. Huang, S.-C. Huang, P. S. Hsu, S. Tanaka, C.-C. Pan, Y. Kawaguchi, K. Fujito, C. G. V. de Walle, J. S. Speck, S. P. DenBaars, S. Nakamura, and D. Feezell, Appl. Phys. Lett. **100**, 201108 (2012).
[5]A. Strittmatter, J. E. Northrup, N. M. Johnson, M. V. Kisin, P. Spiberg, H. El-Ghoroury, A. Usikov, and A. Syrkin, Phys. Status Solidi B **248**, 561 (2011).
[6]J. E. Northrup and J. Neugebauer, Phys. Rev. B **60**, R8473 (1999).
[7]T. Zhu, C. F. Johnston, M. J. Kappers, and R. A. Oliver, J. Appl. Phys. **108**, 083521 (2010).
[8]M. Caliebe, Y. Han, M. Hocker, T. Meisch, C. Humphreys, K. Thonke, and F. Scholz, Phys. Status Solidi B **253**, 46 (2016).
[9]J. Bruckbauer, Z. Li, G. Naresh-Kumar, M. Warzecha, P. R. Edwards, L. Jiu, Y. Gong, J. Bai, T. Wang, C. Trager-Cowan, and R. W. Martin, Sci. Rep. **7**, 10804 (2017).
[10]F. Brunner, F. Edokam, U. Zeimer, W. John, D. Prasai, O. Krüger, and M. Weyers, Phys. Status Solidi B **252**, 1189 (2015).
[11]T. Zhu, D. Sutherland, T. J. Badcock, R. Hao, M. A. Moram, P. Dawson, M. J. Kappers, and R. A. Oliver, Jpn. J. Appl. Phys., Part 1 **52**, 08JB01 (2013).
[12]S. Ploch, T. Wernicke, D. V. Dinh, M. Pristovsek, and M. Kneissl, J. Appl. Phys. **111**, 033526 (2012).
[13]M. Pristovsek, Y. Han, T. Zhu, M. Frentrup, M. J. Kappers, C. J. Humphreys, G. Kozlowski, P. Maaskant, and B. Corbett, Phys. Status Solidi B **252**, 1104 (2015).
[14]D. V. Dinh, M. Akhter, S. Presa, G. Kozlowski, D. O'Mahony, P. P. Maaskant, F. Brunner, M. Caliebe, M. Weyers, F. Scholz, B. Corbett, and P. J. Parbrook, Phys. Status Solidi A **212**, 2196 (2015).
[15]R. Southern-Holland, M. Halsall, T. Wang, and Y. Gong, Phys. Status Solidi C **13**, 274 (2016).
[16]P. R. Edwards and R. W. Martin, Semicond. Sci. Technol. **26**, 064005 (2011).
[17]J. Christen, M. Grundmann, and D. Bimberg, J. Vac. Sci. Technol. **9**, 2358 (1991).
[18]T. Wang, J. Bai, P. J. Parbrook, and A. G. Cullis, Appl. Phys. Lett. **87**, 151906 (2005).
[19]J. Bai, Y. Gong, K. Xing, X. Yu, and T. Wang, Appl. Phys. Lett. **102**, 101906 (2013).
[20]B. Liu, R. Smith, M. Athanasiou, X. Yu, J. Bai, and T. Wang, Appl. Phys. Lett. **105**, 261103 (2014).
[21]Y. Zhang, J. Bai, Y. Hou, R. M. Smith, X. Yu, Y. Gong, and T. Wang, AIP Adv. **6**, 025201 (2016).
[22]R. W. Martin, P. R. Edwards, K. P. O'Donnell, M. D. Dawson, C.-W. Jeon, C. Liu, G. R. Rice, and I. M. Watson, Phys. Status Solidi A **201**, 665 (2004).
[23]P. R. Edwards, L. K. Jagadamma, J. Bruckbauer, C. Liu, P. Shields, D. Allsopp, T. Wang, and R. W. Martin, Microsc. Microanal. **18**, 1212 (2012).
[24]J. Bruckbauer, P. R. Edwards, T. Wang, and R. W. Martin, Appl. Phys. Lett. **98**, 141908 (2011).
[25]D. Drouin, A. R. Couture, D. Joly, X. Tastet, V. Aimez, and R. Gauvin, Scanning **29**, 92 (2007).
[26]M. J. Wallace, P. R. Edwards, M. J. Kappers, M. A. Hopkins, F. Oehler, S. Sivaraya, D. W. E. Allsopp, R. A. Oliver, C. J. Humphreys, and R. W. Martin, J. Appl. Phys. **116**, 033105 (2014).
[27]M. J. Wallace, P. R. Edwards, M. J. Kappers, M. A. Hopkins, F. Oehler, S. Sivaraya, R. A. Oliver, C. J. Humphreys, D. W. E. Allsopp, and R. W. Martin, J. Appl. Phys. **117**, 115705 (2015).
[28]X. Ni, U. Özgür, A. A. Baski, H. Morkoç, L. Zhou, D. J. Smith, and C. A. Tran, Appl. Phys. Lett. **90**, 182109 (2007).
[29]C. G. Bryce, E. D. L. Boulbar, P.-M. Coulon, P. R. Edwards, I. Gîrgel, D. W. E. Allsopp, P. A. Shields, and R. W. Martin, J. Phys. D: Appl. Phys. **50**, 42LT01 (2017).
[30]Y. Matsuda, M. Funato, and Y. Kawakami, Appl. Phys. Express **10**, 071003 (2017).
[31]J. Griffiths, C. X. Ren, P.-M. Coulon, E. Le Boulbar, C. Bryce, I. Gîrgel, A. Howkins, I. Boyd, R. Martin, D. Allsopp, P. Shields, C. Humphreys, and R. Oliver, Appl. Phys. Lett. **110**, 172105 (2017).
[32]M. Hocker, P. Maier, I. Tischer, T. Meisch, M. Caliebe, F. Scholz, M. Mundszinger, U. Kaiser, and K. Thonke, J. Appl. Phys. **121**, 075702 (2017).
[33]E. D. L. Boulbar, I. Gîrgel, C. J. Lewins, P. R. Edwards, R. W. Martin, A. Šatka, D. W. E. Allsopp, and P. A. Shields, J. Appl. Phys. **114**, 094302 (2013).